

Adapting SAM via Cross-Entropy Masking for Class Imbalance in Remote Sensing Change Detection

Humza Naveed^{*†}, Xina Zeng^{*†}, Mitch Bryson^{*†}, Nagita Mehrseresht[‡]

^{*}The University of Sydney [†]ARIAM [‡]NearMap

{hav0885, xzen3830, mitch.bryson}@uni.sydney.edu.au, nagita.mehrseresht@nearmap.com

arXiv:2508.10568v1 [cs.CV] 14 Aug 2025

Abstract—Foundational models have achieved significant success in diverse domains of computer vision. They learn general representations that are easily transferable to tasks not seen during training. One such foundational model is Segment anything model (SAM), which can accurately segment objects in images. We propose adapting the SAM encoder via fine-tuning for remote sensing change detection (RSCD) along with spatial-temporal feature enhancement (STFE) and multi-scale decoder fusion (MSDF) to detect changes robustly at multiple scales. Additionally, we propose a novel cross-entropy masking (CEM) loss to handle high class imbalance in change detection datasets. Our method outperforms state-of-the-art (SOTA) methods on four change detection datasets, Levir-CD, WHU-CD, CLCD, and S2Looking. We achieved 2.5% F1-score improvement on a large complex S2Looking dataset. The code is available at: <https://github.com/humza909/SAM-CEM-CD>

Index Terms—Change Detection, Segment Anything Model, Vision Foundation Models, Remote Sensing

I. INTRODUCTION

Remote sensing change detection (RSCD) identifies changes between pairs of images captured by satellite or aerial imaging at different times. Correctly finding changes is crucial in applications such as future forecasting, environmental monitoring, land cover and land use analysis, and disaster management. RSCD methods have been studied extensively [1]–[4] with approaches ranging from simple feature differentiation [5] to modern deep learning methods [1], [6], [7].

Deep learning methods for change detection often employ the pre-trained weights of models trained on related vision tasks and domains to enhance performance. For example, the pre-trained ResNet backbone [8] was used to train bi-temporal image transformers for change detection (BIT) in [2], the pre-trained VGG [9] backbone was used in change-prior based change detection (CGNET) [6], and data-efficient transformers (deit) [10] were used in Changevit [3]. Although these backbone models are trained for different domains, their pre-learned features fine-tune well for remote sensing change detection, yielding significant performance gains compared to training these models from scratch [2], [3], [6]. Recently, the performance gains achieved by foundational models have attracted researchers to adapt them for change detection [11], [12]; for example, remote-clip’s [13] encoder was used in conjunction with change detection architectures [1], [2] to improve change detection performance. Most of the pre-trained models described above are trained for non-dense



Fig. 1: An illustration of dropped pixels in cross-entropy masking to handle class imbalance. The first three images are input images and ground truth, while the last image is an overlay with red pixels representing those dropped during loss calculation.

prediction tasks, such as image classification as opposed to image segmentation. Pixel-wise change detection is a dense segmentation task and the features extracted by encoders trained for similar dense spatial tasks are expected to be more effective for change detection. To this end, the Segment Anything Model (SAM) [14], [15] a foundational model for image segmentation was adapted for change detection in [11]. This work freezes the FastSAM (a smaller and faster variant of SAM) [15] encoder and trains an adapter and decoder from scratch, processing bi-temporal images sequentially and fusing them before classification.

This paper presents a new architecture for change detection that also utilizes pre-trained FastSAM. We extract multi-scale features from the feature pyramid network in FastSAM [15] for bi-temporal images. We employ a spatial-temporal feature enhancement (STFE) branch to learn cross-temporal relations at each scale. The output of the STFE branch is forwarded to a UNet-style decoder [16] followed by multi-scale decoder fusion (MSDF) and a residual head for change map classification. As opposed to [11], the encoder in our architecture uses the foundational model’s encoder connected in shared encoder/twin-style. Our use of fine-tuning on the FastSAM encoder outperforms change detection frameworks based on encoders using non-dense prediction models in [2], [6], as empirically evident in our experiments.

RSCD is a highly class imbalance problem, where pixels of change are significantly less frequent than non-change pixels. This class imbalance introduces an inherent bias in the learning process in which models emphasize improving the accuracy of non-change areas over areas of change. To address this, we propose a novel way of masking non-change pixels during

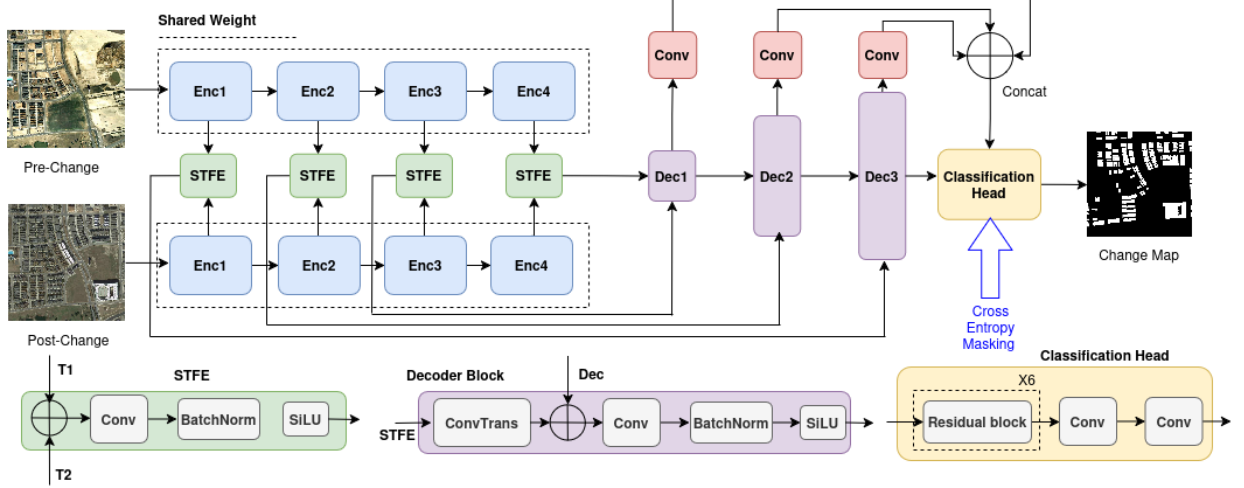


Fig. 2: The architectural diagram of SAM-CEM-CD, X6 in classification head represents six repetitions of the residual module.

the loss calculation, called cross-entropy masking (CEM), interchangeably cross-entropy dropout, shown in Figure 1.

The key contributions of our work are:

- Proposing a SAM-based change detection architecture that learns cross-temporal multi-scale feature relations through STFE and MSDF for accurate change map classification.
- We propose incorporating an encoder from a pre-trained model for dense image segmentation and fine-tuning it for change detection instead of using non-dense prediction models.
- We propose a novel way to deal with class imbalance in change detection by masking or dropping non-change pixels in the ground-truth, naming it cross-entropy masking (CEM).

The rest of the paper is organized as follows: Section II discusses the proposed method, Section III discusses experimentation and results, followed by the conclusion in Section IV.

II. PROPOSED METHOD

A. Siamese FastSAM Encoder

FastSAM [15] is a smaller and faster instance segmentation model compared to segment anything [14]. It contains Yolov8-seg architecture trained on only 2% of SAM's data, achieving equivalent performance. The FastSAM consists of encoder-decoder architecture, where the encoder encodes the input image into a compressed representation merging multi-scale features through a feature pyramid network. Due to dense image segmentation training, feature representations learned by the encoder are better transferable to change segmentation maps than the ResNet or vision transformer models trained for classification as in [3], [6]. Our method adapts the FastSAM encoder by fine-tuning it for change detection in a Siamese-style architecture with weight sharing.

Given a set of two remote sensing images I_1 and I_2 for change detection, we process the images through the encoder. We extract four feature maps F_1, F_2, F_3 , and F_4 from the encoder at four scales 1/4, 1/8, 1/16, and 1/32. The scale 1/4 is

extracted from the CNN backbone of FastSAM, where the remaining feature maps are taken from the feature pyramid network.

B. Spatial-Temporal Feature Enhancement

We concatenate spatiotemporal representations and process them through transformations to learn cross-temporal relations and differences in feature maps, shown in Figure 2. Our spatial-temporal feature enhancement (STFE) module is represented by:

$$F_{STFE} = SiLU(BN(Conv2D_{3x3}(F_i^{pre}, F_i^{post}))) \quad (1)$$

where F_{STFE} are the enhanced feature maps, F_i^{pre} and F_i^{post} are pre-change and post-change images, respectively, $Conv2D$ is 2D convolution, BN is batch normalization, and $SiLU$ is sigmoid linear unit activation function. The STFE module is replicated four times for feature maps at each scale extracted from the encoder. The enhanced representations are forwarded to the decoder for change detection.

C. Unet Decoder

Multi-scale change features from the STFE module are used to reconstruct the change map in the UNet-style decoder [16]. The feature map resolution in the decoder gradually increases with skip connections, concatenating features from the STFE with the decoder output. The decoder block is written as:

$$F_{up} = ConvTrans2D_{2x2}(F_{STFE}) \quad (2)$$

$$F_{out} = SiLU(BN(Conv2D_{3x3}(F_{up}, F_{dec})))$$

In equation 2, the feature map from the difference branch (alternatively, STFE) F_{STFE} is upsampled F_{up} with transpose convolution $ConvTrans2D_{2x2}$ of kernel size 2×2 to match the spatial resolution of the decoder output. The F_{up} is concatenated with the previous output of the decoder to process through the next decoder block, providing contextual information on changes in the bitemporal images. For architectural consistency, we ensure that the decoder block has the

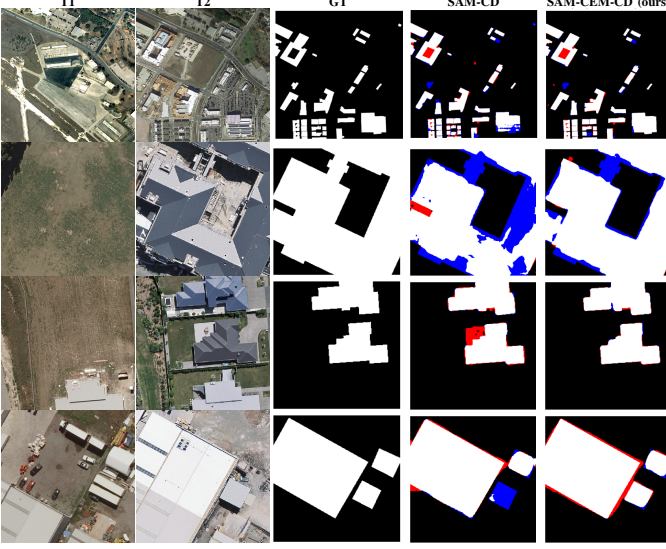


Fig. 3: Comparison of change detection results. T1 and T2 are the input images at different timestamps, GT is the ground truth, and SAM-CD [11] and SAM-CEM-CD (ours) are predictions from models. Red pixels are FPs and blue pixels are FNs.

convolution, batch normalization, and activation function in the same order as in the FastSAM encoder and the STFE module as given in equation 1.

D. Multi-Scale Decoder Fusion and Change Map

The early layers of the decoder contain rich global semantic information, whereas the last layers have local change structural detail. The decoder processes this information at multi-spatial resolutions, taking into account objects and changes in the temporal images at different scales. We collect every decoder block output, fuse it, and forward it to the classification head for change detection. Our classification head contains residual blocks followed by a convolution layer for the change map, as depicted in Figure 2.

E. Cross-Entropy Masking for Class Imbalance

The bitemporal change detection datasets are heavily imbalanced in change and unchanged regions. For instance, Levir-CD and WHU-CD have 95% unchanged pixels and only 5% change pixels. Because of this imbalance, the cross-entropy loss in change detection is highly biased towards accurately classifying unchanged pixels instead of change pixels. To ensure that the model emphasizes change pixels as equally as unchanged pixels, we randomly dropout the unchanged pixels from the binary cross-entropy loss. For this, we compute the per-element binary cross-entropy (BCE) as mentioned:

$$L_{bce} = -y_i \log(\hat{y}_i) + (1 - y_i) \log(1 - \hat{y}_i) \quad (3)$$

where y_i is the ground-truth and \hat{y}_i is the predicted label. To dropout the pixels in binary cross-entropy, we create a mask by keeping all the loss values for change pixels and dropping

values for the unchanged pixels based on the dropout value. This can be written as follows:

$$M_i = \begin{cases} 1 & \text{if } y_i = 1 \\ 1 & \text{if } y_i = 0 \text{ and } (R_i > \delta) \\ 0 & \text{if } y_i = 0 \text{ and } (R_i < \delta) \end{cases} \quad (4)$$

In equation 4, R_i is a matrix of the same dimensions as the change map with values sampled from the Uniform distribution function i.e. $R_i \sim \text{Uniform}(0, 1)$. The δ in equation 4 is the dropout probability that defines the number of unchanged pixels to drop from loss calculation. The overall binary cross-entropy loss function with dropout becomes:

$$L_{drop} = \frac{\sum_{i=1}^N L_{bce} \cdot M_i}{\sum_{i=1}^N M_i} \quad (5)$$

III. EXPERIMENTATION AND RESULTS

A. Implementation Details

We used PyTorch for the model training. We trained the model for 35 epochs using a stochastic gradient descent (SGD) optimizer. We use the FastSAM encoder and fine-tune its pre-trained weights. The learning rate (lr) is 0.01 for Levir-CD and CLCD, and 0.001 for WHU-CD and S2Looking. We decay the learning rate in each iteration $lr * (1 - \text{iterations}/50)^{\text{decay}}$, where decay is 2.0 for Levir-CD and CLCD, and 3.0 for WHU-CD and S2Looking. Image flipping and random cropping augmentations are applied during training and images are flipped 4 times for inference to produce stable results. More details can be seen in our GitHub repo: <https://github.com/humza909/SAM-CEM-CD>.

B. Change Detection Datasets

The following datasets are used for training and testing of our change detection framework:

1) *Levir-CD* [20]: This dataset contains 637 image pairs with 31,333 annotated change objects. The data is collected from Google Earth for six Texas cities between 2012 and 2016. It has 445 training, 64 validation, and 128 testing images.

2) *WHU-CD* [21]: This is an aerial imaging dataset captured over Christchurch, New Zealand, after the 2011 earthquake, between 2012-2016. We used the dataset split of 6096 training, 762 validation, and testing images provided by [11].

3) *CLCD* [22]: The cropland change detection dataset is captured in Guangdong, China between 2017 to 2019. It consists of 600 image pairs collected by the Gaofen-2 satellite with a split of 320 training, 120 validation and testing image pairs.

4) *S2Looking* [23]: This is a large-scale change detection dataset with 5000 image pairs collected from satellites such as Gaofen, SuperView, and BeiJing-2. The dataset offers various challenges like misalignment and varying poses.

C. Evaluation Metrics

To evaluate the performance of our model, we employ widely used metrics for change detection, including precision (Prec), recall (Rec), F_1 score, overall accuracy (OA), and intersection over union (IoU). The formulas are the same as given in [11].

TABLE I: Quantitative results of different RSCD methods on the Levir-CD and WHU-CD datasets, results are in %. The best results are highlighted.

Method	Levir-CD					WHU-CD				
	Pre	Rec	OA	mF_1	$mIoU$	Pre	Rec	OA	mF_1	$mIoU$
FC-Siam-diff [7]	92.93	87.02	98.15	89.73	82.67	94.52	89.32	98.70	91.74	85.65
FC-Siam-conc [7]	92.03	89.82	98.28	90.89	84.34	93.94	92.83	98.90	93.37	88.19
SNUNet [17]	93.83	90.11	98.50	91.88	85.84	92.61	83.26	98.10	87.30	79.40
BIT [2]	90.27	83.37	97.60	86.46	78.23	87.92	93.41	98.29	90.46	83.72
ChangeFormer [1]	91.46	86.31	97.95	88.69	81.21	96.28	92.95	99.12	94.55	90.08
CTD-Former [4]	93.60	91.85	98.62	92.71	87.11	96.74	97.03	99.50	96.89	94.11
CGNet [6]	95.95	94.95	99.13	95.44	91.58	98.04	96.14	99.52	97.07	94.44
EATDer [18]	96.29	92.70	98.87	94.41	89.84	95.57	93.06	99.01	94.28	89.64
SAM-CD [11]	95.87	95.14	99.14	95.50	91.68	96.91	95.42	99.36	96.15	92.81
SAM-CEM-CD (ours)	96.12	95.84	99.23	95.98	92.51	97.45	97.19	99.54	97.23	94.73

TABLE II: Quantitative results of different RSCD methods on the CLCD dataset, results are in %.

Method	Accuracy Metrics				
	Pre	Rec	OA	mF_1	$mIoU$
FC-Siam-diff [7]	83.13	74.60	94.73	78.10	68.19
FC-Siam-conc [7]	81.65	79.94	94.84	80.77	70.98
SNUNet [17]	85.92	82.62	95.84	84.19	75.11
BIT [2]	81.42	70.27	94.17	74.39	64.51
ChangeFormer [1]	84.41	81.36	95.47	82.80	73.40
CTD-Former [4]	87.29	83.17	96.12	85.08	76.24
CGNet [6]	85.87	85.30	96.00	85.58	76.83
EATDer [18]	87.16	77.18	93.84	81.16	71.18
SAM-CD [11]	88.25	85.65	96.26	86.89	78.53
SAM-CEM-CD (ours)	88.71	86.89	96.71	87.76	79.77

TABLE III: Quantitative results of different RSCD methods on the S2Looking dataset for change class, results are in %.

Method	Accuracy Metrics			
	Pre	Rec	F_1	IoU
FC-Siam-diff [7]	83.49	32.32	46.60	30.38
FC-Siam-conc [7]	68.27	18.52	13.54	-
SNUNet [17]	45.26	50.60	47.78	31.39
BIT [2]	70.26	56.53	62.65	45.62
ChangeFormer [1]	72.82	56.13	63.39	-
CGNet [6]	70.18	59.38	64.33	47.41
EATDer [18]	65.85	54.74	59.78	42.64
SAM-CD [11]	72.80	58.92	65.13	48.29
SAM-CEM-CD (ours)	73.20	63.02	67.73	51.19

D. Quantitative Results

Our method, SAM-CEM-CD, achieves superior performance than other SOTA methods in the literature. For the correctness of the results, we ran our experiments three times for each dataset and averaged the results. The results for other methods in Tables I, II, and III are collected from [11]. Table I shows an increase of 0.48% and 0.83% in mF_1 and $mIoU$, respectively, for the Levir-CD dataset. Similarly, we achieve 97.23% mF_1 and 94.73% $mIoU$ for the WHU-CD dataset, compared to the second-best CGNET [6], which yields 97.07% mF_1 and 94.44% $mIoU$. We recalculated SAM-CD results for WHU-CD as given in Table I. Table II shows an approximately 1% improvement in mF_1 and $mIoU$ for CLCD against other methods, whereas for S2Looking we achieve 2.5% better performance than the SOTA methods in Table III.

TABLE IV: Ablation study using different modules in our architecture on the Levir-CD dataset, results are in %. STFE stands for spatio-temporal feature enhancement, D stands for Unet-decoder, MSDF stands for multi-scale decoder fusion, and CEM stands for cross-entropy masking.

Method	mF_1	$mIoU$
SAM + STFE + D	95.87	92.32
SAM + STFE + D + MSDF	95.92	92.38
SAM + STFE + D + MSDF + CEM	95.98	92.51

TABLE V: Ablation study using different masking probability values on the Levir-CD dataset, results are in %, and δ is the masking ratio.

Metric	$\delta = 0.2$	$\delta = 0.3$	$\delta = 0.4$	$\delta = 0.5$	$\delta = 0.6$
mF_1	95.93	95.98	95.94	95.86	95.80
$mIoU$	92.41	92.51	92.44	92.29	92.19

E. Visualization

We visually compare the change maps of SAM-CD and SAM-CEM-CD in Figure 3. The blue predictions are FNs, and the red predictions are FPs. We can see the reduced FNs and FPs by SAM-CEM-MCD in the figure, which shows the significance of our method over other SOTA methods.

F. Ablation Study

In this section, we examine the impact of various architectural components on performance.

1) *Cross-Entropy Masking Ratio*: Cross-entropy masking balances the impact of a highly imbalanced class ratio in change detection datasets. However, finding a reasonable masking ratio is important for optimal network performance. Higher values of masking can lead to removing too much information for the network to learn, while low values can lead to cross-entropy masking performing equivalent to cross-entropy. We show an analysis of different masking ratios in Table V and found that masking probability δ equal to 0.3 is optimal.

2) *Architectural Modules*: We compared the impact of various modules in our architecture. We show the improvement in performance achieved due to STFE, MSDF, and CEM in Table IV, where the final architecture with all the modules performs better than all the other configurations.

TABLE VI: Ablation study using different losses for class imbalance on the Levir-CD dataset, results are in %.

Method	mF_1	$mIoU$
BCE ($= 0.7$) + Dice ($= 0.3$)	95.74	92.08
Focal ($\alpha = 0.5$, $\gamma = 2.0$)	95.78	92.16
Weighted-BCE ($w_0 = 0.7$, $w_1 = 1.0$)	95.87	92.31
Weighted-BCE ($w_0 = 0.3$, $w_1 = 0.7$)	95.66	91.95
CEM ($\delta = 0.3$)	95.98	92.51

TABLE VII: Ablation study using different pre-trained models in our methodology on the Levir-CD dataset with and without CEM, results are in %,

Method	mF_1	$mIoU$	mF_1 (CEM)	$mIoU$ (CEM)
VGG-16 [9]	95.10	91.00	95.33	91.38
ResNet-101 [8]	95.08	90.96	95.31	91.34
ResNet-152 [8]	95.09	90.98	95.39	91.48
WideResNet-101-2 [19]	95.00	90.83	95.01	90.84
Ours	95.92	92.38	95.98	92.51

3) *Losses for Class Imbalance*: We compared cross-entropy masking (CEM) with other losses widely used for class imbalance, including focal loss [24], a combination of binary cross-entropy and dice loss [25], and weighted binary cross-entropy [25] in Table VI. Compared with these, CEM performs the best, whereas weighted-BCE is the second best.

4) *Pre-trained Model Comparison*: A comparison between pre-trained models for non-dense prediction tasks [8], [9], [19] against dense prediction tasks [14], [15] is shown in Table VII. We replaced the encoder in Figure 2 with encoders of various pre-trained models. We can see the model trained from image segmentation outperforms others.

IV. CONCLUSION

This paper presents employing the dense prediction SAM foundational model for change detection. We proposed spatial-temporal feature enhancement (STFE) and multi-scale decoder fusion (MSDF) architectural modules to enhance the detection performance. Our novel cross-entropy masking (CEM) loss achieved large gains over other losses suggested for class imbalance. Overall, we showed using an encoder from pre-trained models for dense prediction tasks along with CEM is an effective architectural design that outperforms SOTA methods.

ACKNOWLEDGEMENT

This work was supported by the ARC Research Hub in Intelligent Robotic Systems for Real-Time Asset Management (IH210100030).

REFERENCES

- [1] W. G. C. Bandara and V. M. Patel, “A transformer-based siamese network for change detection,” pp. 207–210, 2022.
- [2] H. Chen, Z. Qi, and Z. Shi, “Remote sensing image change detection with transformers,” *IEEE Transactions on Geoscience and Remote Sensing*, vol. 60, pp. 1–14, 2021.
- [3] D. Zhu, X. Huang, H. Huang, Z. Shao, and Q. Cheng, “Changevit: Unleashing plain vision transformers for change detection,” *arXiv preprint arXiv:2406.12847*, 2024.
- [4] K. Zhang, X. Zhao, F. Zhang, L. Ding, J. Sun, and L. Bruzzone, “Relation changes matter: Cross-temporal difference transformer for change detection in remote sensing images,” *IEEE Transactions on Geoscience and Remote Sensing*, 2023.
- [5] D. Lu, P. Mausel, E. Brondizio, and E. Moran, “Change detection techniques,” *International journal of remote sensing*, vol. 25, no. 12, pp. 2365–2401, 2004.
- [6] C. Han, C. Wu, H. Guo, M. Hu, J. Li, and H. Chen, “Change guiding network: Incorporating change prior to guide change detection in remote sensing imagery,” *IEEE Journal of Selected Topics in Applied Earth Observations and Remote Sensing*, 2023.
- [7] R. C. Daudt, B. Le Saux, and A. Boulch, “Fully convolutional siamese networks for change detection,” in *2018 25th IEEE International Conference on Image Processing (ICIP)*. IEEE, 2018, pp. 4063–4067.
- [8] K. He, X. Zhang, S. Ren, and J. Sun, “Deep residual learning for image recognition,” in *Proceedings of the IEEE conference on computer vision and pattern recognition*, 2016, pp. 770–778.
- [9] K. Simonyan and A. Zisserman, “Very deep convolutional networks for large-scale image recognition,” *arXiv preprint arXiv:1409.1556*, 2014.
- [10] H. Touvron, M. Cord, M. Douze, F. Massa, A. Sablayrolles, and H. Jégou, “Training data-efficient image transformers & distillation through attention,” in *International conference on machine learning*. PMLR, 2021, pp. 10347–10357.
- [11] L. Ding, K. Zhu, D. Peng, H. Tang, K. Yang, and L. Bruzzone, “Adapting segment anything model for change detection in vhr remote sensing images,” *IEEE Transactions on Geoscience and Remote Sensing*, 2024.
- [12] K. Li, X. Cao, and D. Meng, “A new learning paradigm for foundation model-based remote-sensing change detection,” *IEEE Transactions on Geoscience and Remote Sensing*, vol. 62, pp. 1–12, 2024.
- [13] F. Liu, D. Chen, Z. Guan, X. Zhou, J. Zhu, Q. Ye, L. Fu, and J. Zhou, “Remoteclip: A vision language foundation model for remote sensing,” *IEEE Transactions on Geoscience and Remote Sensing*, 2024.
- [14] A. Kirillov, E. Mintun, N. Ravi, H. Mao, C. Rolland, L. Gustafson, T. Xiao, S. Whitehead, A. C. Berg, W.-Y. Lo *et al.*, “Segment anything,” *arXiv preprint arXiv:2304.02643*, 2023.
- [15] X. Zhao, W. Ding, Y. An, Y. Du, T. Yu, M. Li, M. Tang, and J. Wang, “Fast segment anything,” *arXiv preprint arXiv:2306.12156*, 2023.
- [16] O. Ronneberger, P. Fischer, and T. Brox, “U-net: Convolutional networks for biomedical image segmentation,” in *Medical image computing and computer-assisted intervention–MICCAI 2015: 18th international conference, Munich, Germany, October 5–9, 2015, proceedings, part III* 18. Springer, 2015, pp. 234–241.
- [17] S. Fang, K. Li, J. Shao, and Z. Li, “Snunet-cd: A densely connected siamese network for change detection of vhr images,” *IEEE Geoscience and Remote Sensing Letters*, vol. 19, pp. 1–5, 2021.
- [18] J. Ma, J. Duan, X. Tang, X. Zhang, and L. Jiao, “Eatder: Edge-assisted adaptive transformer detector for remote sensing change detection,” *IEEE Transactions on Geoscience and Remote Sensing*, 2023.
- [19] S. Zagoruyko and N. Komodakis, “Wide residual networks,” *arXiv preprint arXiv:1605.07146*, 2016.
- [20] H. Chen and Z. Shi, “A spatial-temporal attention-based method and a new dataset for remote sensing image change detection,” *Remote sensing*, vol. 12, no. 10, p. 1662, 2020.
- [21] S. Ji, S. Wei, and M. Lu, “Fully convolutional networks for multisource building extraction from an open aerial and satellite imagery data set,” *IEEE Transactions on geoscience and remote sensing*, vol. 57, no. 1, pp. 574–586, 2018.
- [22] J. Yang and X. Huang, “30 m annual land cover and its dynamics in china from 1990 to 2019,” *Earth System Science Data Discussions*, vol. 2021, pp. 1–29, 2021.
- [23] L. Shen, Y. Lu, H. Chen, H. Wei, D. Xie, J. Yue, R. Chen, S. Lv, and B. Jiang, “S2looking: A satellite side-looking dataset for building change detection,” *Remote Sensing*, vol. 13, no. 24, p. 5094, 2021.
- [24] T.-Y. Lin, P. Goyal, R. Girshick, K. He, and P. Dollár, “Focal loss for dense object detection,” in *Proceedings of the IEEE international conference on computer vision*, 2017, pp. 2980–2988.
- [25] S. Jadon, “A survey of loss functions for semantic segmentation,” in *2020 IEEE conference on computational intelligence in bioinformatics and computational biology (CIBCB)*. IEEE, 2020, pp. 1–7.